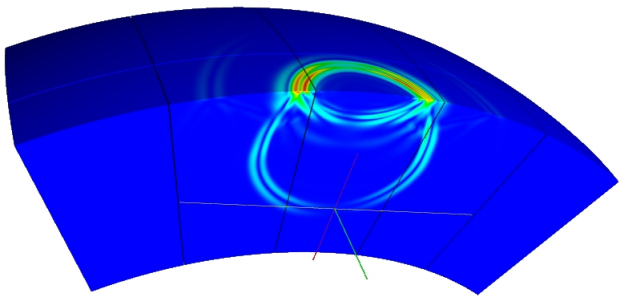

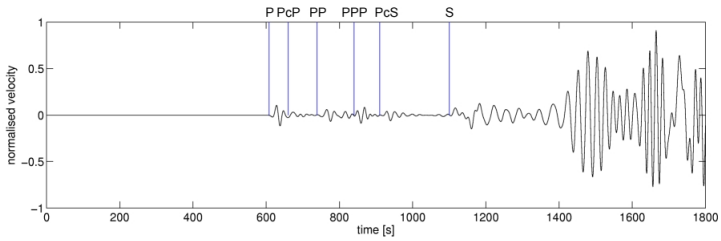

fd3s - Documentation

Andreas Fichtner
Tarje Nissen-Meyer
Heiner Igel

July 29, 2006

Contents

1 The analytical setup **4**
1.1 Equations of motion 4
1.2 Anisotropy 5
1.2.1 SH and SV waves in spherical coordinates 6
1.2.2 PH and PV waves in spherical coordinates 8
1.3 Anelasticity 8

2 Discretisation **12**
2.1 Discretisation in space 12
2.2 Discretisation in time 12
2.3 The free surface 14
2.4 Absorbing boundaries 16

3 Implementation and technical details **17**
3.1 Directory structure 17
3.2 Source code 17
3.3 Input files 18
3.4 Parallelisation 18
3.5 Output files 19

4 Evaluation **20**
4.1 Numerical body wave dispersion 20
4.2 Elastic waves in the Preliminary Reference Earth Model (PREM) 23

A Appendix A - Dispersion measurements **25**

Abstract

This is the documentation of `fd3s`, a finite-difference solver of the elastic wave equation in a spherical section. The programme allows to include both attenuation and anisotropy with radial symmetry axis.
The documentation is organised as follows: We start with a detailed formulation of the analytical problem. Special attention is given to the modelling of anisotropy and attenuation. Then, we proceed with a description of the spatio-temporal discretisation scheme with an emphasis on the implementation of the free surface and absorbing boundary conditions. We conclude with a brief overview of the Fortan source code and some technical details.
A previous version of `fd3s` was presented by Nissen-Meyer (2001) and applied to the elastic wave propagation through subduction zones by Igel et al. (2002).

1 The analytical setup

1.1 Equations of motion

The programme `fd3s` solves the linearised momentum equation, given by

$$\rho(\mathbf{x})\partial_t \mathbf{v}(\mathbf{x},t) - \nabla\cdot\boldsymbol{\sigma}(\mathbf{x},t) = \mathbf{f}(\mathbf{x},t) \tag{1}$$

and subject to the free-surface boundary condition

$$\boldsymbol{\sigma}\cdot\mathbf{e}_r|_{r=R} = \mathbf{0}\,. \tag{2}$$

In equation (1) the symbols $\mathbf{v}$ and $\boldsymbol{\sigma}$ denote the velocity field and the stress tensor, respectively. The external force density is symbolised by $\mathbf{f}$, and ρ is the mass density of the steady-state configuration. Physically, equation (1) means that inertial and stress-induced forces are balanced by body forces. The free surface condition (2) requires the normal stresses to vanish at the Earth's surface, i.e., et $r = R$, where R is the radius of the Earth which is assumed to be perfectly spherical. In order to obtain a complete set of equations, the stress tensor has to be related to the velocity field. It is usually assumed that the rheology is anelastic, i.e., that the stress rate $\partial_t\boldsymbol{\sigma}$ depends linearly on the entire past history of the strain rate $\partial_t\boldsymbol{\epsilon}$:

$$\partial_t\boldsymbol{\sigma}(\mathbf{x},t) = \int_{-\infty}^{\infty} \dot{\mathbf{C}}(\mathbf{x},t-t') : \dot{\boldsymbol{\epsilon}}(\mathbf{x},t')\,dt'\,, \tag{3}$$

where

$$\dot{\boldsymbol{\epsilon}} := \frac{1}{2}\left[(\nabla\mathbf{v}) + (\nabla\mathbf{v})^T\right]\,. \tag{4}$$

The fourth order tensor $\mathbf{C}$ is the elastic tensor with its symmetries

$$C_{ijkl} = C_{klij} = C_{jikl}\,. \tag{5}$$

A detailed derivation of equations (1) to (5) can be found for example in Dahlen & Tromp (1998). It is important to note that the linear dependence of stress rate on strain rate history is not a physical necessity as for example the momentum conservation (1). However, it has been verified for a number of materials that are thought to be the principal constituents of the Earth's mantle (e.g. Jackson, 2000).
Since we are interested in the solution in a spherical section (see figure 1), it is convenient to compute $\nabla\cdot\boldsymbol{\sigma}$ and $\dot{\boldsymbol{\epsilon}}$ in spherical coordinates (e.g. Schade, 1999):

$$(\nabla\cdot\boldsymbol{\sigma})_r = \partial_r\sigma_{rr} + \frac{1}{r\sin\theta}\partial_\varphi\sigma_{\varphi r} + \frac{1}{r}\partial_\theta\sigma_{\theta r} + \frac{1}{r}(2\sigma_{rr} + \sigma_{\theta r}\cot\theta - \sigma_{\varphi\varphi} - \sigma_{\theta\theta})\,, \tag{6a}$$

$$(\nabla\cdot\boldsymbol{\sigma})_\varphi = \partial_r\sigma_{\varphi r} + \frac{1}{r\sin\theta}\partial_\varphi\sigma_{\varphi\varphi} + \frac{1}{r}\partial_\theta\sigma_{\theta\varphi} + \frac{1}{r}(3\sigma_{r\varphi} + 2\sigma_{\theta\varphi}\cot\theta)\,, \tag{6b}$$

$$(\nabla\cdot\boldsymbol{\sigma})_\theta = \partial_r\sigma_{r\theta} + \frac{1}{r\sin\theta}\partial_\varphi\sigma_{\varphi\theta} + \frac{1}{r}\partial_\theta\sigma_{\theta\theta} + \frac{1}{r}(3\sigma_{r\theta} + \sigma_{\theta\theta}\cot\theta - \sigma_{\varphi\varphi}\cot\theta)\,, \tag{6c}$$

$$\dot{\epsilon}_{rr} = \partial_r v_r\,, \tag{7a}$$

$$\dot{\epsilon}_{r\varphi} = \frac{1}{2}\left(\partial_r v_\varphi + \frac{1}{r\sin\theta}\partial_\varphi v_r - \frac{1}{r}v_\varphi\right)\,, \tag{7b}$$

$$\dot{\epsilon}_{r\theta} = \frac{1}{2}\left(\partial_r v_\theta + \frac{1}{r}\partial_\theta v_r - \frac{1}{r}v_\theta\right)\,, \tag{7c}$$

$$\dot{\epsilon}_{\varphi\varphi} = \frac{1}{r}\left(\frac{1}{\sin\theta}\partial_\varphi v_\varphi + v_r + v_\theta\cot\theta\right)\,, \tag{7d}$$

$$\dot{\epsilon}_{\varphi\theta} = \frac{1}{2r}\left(\frac{1}{\sin\theta}\partial_\varphi v_\theta - v_\varphi\cot\theta + \partial_\theta v_\varphi\right)\,, \tag{7e}$$

$$\dot{\epsilon}_{\theta\theta} = \frac{1}{r}\partial_\theta v_\theta + \frac{1}{r}v_r\,. \tag{7f}$$

In equations (6a) to (7f) the symbols r, φ, θ denote the radius, longitude and colatitude, respectively. Note that $\dot{\boldsymbol{\epsilon}}$ is symmetric.
It remains to clarify the particular form of the elastic tensor $\mathbf{C}$ in equation (3). That means that the anisotropy and the form of anelasticity have to be specified.

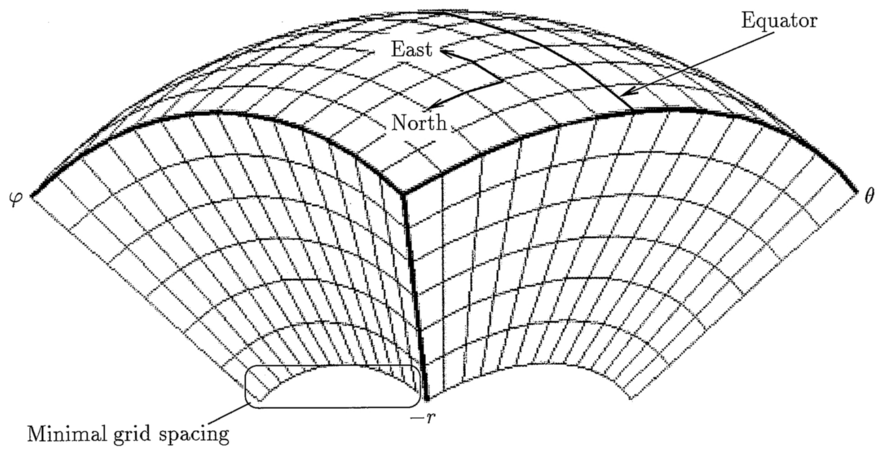

Figure 1: Spherical section excluding the centre. The variables r, θ and φ denote the radius, colatitude and longitude, respectively. Picture taken from Nissen-Meyer, 2001.

1.2 Anisotropy

Anisotropy is the dependence of the elastic tensor on the orientation of the coordinate system. In seismological terms, anisotropy is the dependence of seismic velocities on the propagation direction and polarisation of an elastic wave. It is thought to play a major role especially in the Earth's crust and upper mantle.

Besides the splitting of shear waves, the so-called Love wave-Rayleigh wave discrepancy is one of the principal seismic observations that is directly related to anisotropy: A Love wave and a Rayleigh wave travelling in the same direction usually exhibit different wave speeds due their different polarisations. This led to the inclusion of anisotropy with radial symmetry axis into the global reference model PREM (Dziewonski & Anderson, 1981). In this model the anisotropy is limited to the upper 220 km. Interestingly, the azimuthal dependence of seismic wave speeds seems to play a minor role in the upper mantle of the Earth, the only notable exception being the upper mantle under the Pacific (Eckström & Dziewonski, 1998).

Guided by these observations, we decided to implement anisotropy with radial symmetry axis in `fd3s`. For such a medium, there are only 5 independent elastic tensor components that are different from zero. Due to the symmetry relations (5) they can be summarised in a 6×6 matrix (e.g. Babuska & Cara, 1991):

$$\begin{pmatrix} c_{rrrr} & c_{rr\varphi\varphi} & c_{rr\theta\theta} & c_{rr\varphi\theta} & c_{rrr\theta} & c_{rrr\varphi} \\ c_{\varphi\varphi rr} & c_{\varphi\varphi\varphi\varphi} & c_{\varphi\varphi\theta\theta} & c_{\varphi\varphi\varphi\theta} & c_{\varphi\varphi r\theta} & c_{\varphi\varphi r\varphi} \\ c_{\theta\theta rr} & c_{\theta\theta\varphi\varphi} & c_{\theta\theta\theta\theta} & c_{\theta\theta\varphi\theta} & c_{\theta\theta r\theta} & c_{\theta\theta r\varphi} \\ c_{\varphi\theta rr} & c_{\varphi\theta\varphi\varphi} & c_{\varphi\theta\theta\theta} & c_{\varphi\theta\varphi\theta} & c_{\varphi\theta r\theta} & c_{\varphi\theta r\varphi} \\ c_{r\theta rr} & c_{r\theta\varphi\varphi} & c_{r\theta\theta\theta} & c_{r\theta\varphi\theta} & c_{r\theta r\theta} & c_{r\theta r\varphi} \\ c_{r\varphi rr} & c_{r\varphi\varphi\varphi} & c_{r\varphi\theta\theta} & c_{r\varphi\varphi\theta} & c_{r\varphi r\theta} & c_{r\varphi r\varphi} \end{pmatrix}$$

$$= \begin{pmatrix} \lambda+2\mu & \lambda+C & \lambda+C & 0 & 0 & 0 \\ \lambda+C & \lambda+2\mu+A & \lambda+A & 0 & 0 & 0 \\ \lambda+C & \lambda+A & \lambda+2\mu+A & 0 & 0 & 0 \\ 0 & 0 & 0 & \mu & 0 & 0 \\ 0 & 0 & 0 & 0 & \mu+B & 0 \\ 0 & 0 & 0 & 0 & 0 & \mu+B \end{pmatrix} \tag{8}$$

Love (1892) proposed an alternative parametrisation

$$\begin{pmatrix} c_{rrrr} & c_{rr\varphi\varphi} & c_{rr\theta\theta} & c_{rr\varphi\theta} & c_{rrr\theta} & c_{rrr\varphi} \\ c_{\varphi\varphi rr} & c_{\varphi\varphi\varphi\varphi} & c_{\varphi\varphi\theta\theta} & c_{\varphi\varphi\varphi\theta} & c_{\varphi\varphi r\theta} & c_{\varphi\varphi r\varphi} \\ c_{\theta\theta rr} & c_{\theta\theta\varphi\varphi} & c_{\theta\theta\theta\theta} & c_{\theta\theta\varphi\theta} & c_{\theta\theta r\theta} & c_{\theta\theta r\varphi} \\ c_{\varphi\theta rr} & c_{\varphi\theta\varphi\varphi} & c_{\varphi\theta\theta\theta} & c_{\varphi\theta\varphi\theta} & c_{\varphi\theta r\theta} & c_{\varphi\theta r\varphi} \\ c_{r\theta rr} & c_{r\theta\varphi\varphi} & c_{r\theta\theta\theta} & c_{r\theta\varphi\theta} & c_{r\theta r\theta} & c_{r\theta r\varphi} \\ c_{r\varphi rr} & c_{r\varphi\varphi\varphi} & c_{r\varphi\theta\theta} & c_{r\varphi\varphi\theta} & c_{r\varphi r\theta} & c_{r\varphi r\varphi} \end{pmatrix}$$

$$= \begin{pmatrix} C_L & F_L & F_L & 0 & 0 & 0 \\ F_L & A_L & A_L - 2N_L & 0 & 0 & 0 \\ F_L & A_L - 2N_L & A_L & 0 & 0 & 0 \\ 0 & 0 & 0 & N_L & 0 & 0 \\ 0 & 0 & 0 & 0 & L_L & 0 \\ 0 & 0 & 0 & 0 & 0 & L_L \end{pmatrix} \tag{9}$$

We chose to use the parametrisation from equation (8) because it easily allows us to model isotropy by simply setting $A = B = C = 0$. Remember, that all components of the elastic tensor are functions of t and $\mathbf{x}$.

1.2.1 SH and SV waves in spherical coordinates

SH and SV waves are horizontally propagating S waves with horizontal and vertical polarisation, respectively. In anisotropic media these two types of waves exhibit different wave speeds. This phenomenon is observed in the Earth's upper mantle.
An exact derivation of the SH and SV wave speeds in spherical coordinates is difficult, but some approximations allow us to obtain simple and useful formulas. We first restrict our attention to a small volume around $(r, \phi, \theta) = (r_0, 0, \pi/2)$. Under this assumption we find the approximations

$$\partial_\phi \approx r_0 \partial_y \,, \quad \partial_\theta \approx -r_0 \partial_z \,, \quad \partial_r \approx \partial_x \,. \tag{10}$$

This allows us to simplify the relations (6a) to (6c) and (7a) to (7f), given that r_0 is very large compared to the maximum stress values:

$$(\nabla \cdot \boldsymbol{\sigma})_r \approx \partial_{rr} + \frac{1}{r_0}(\partial_\phi \sigma_{\phi r} + \partial_\theta \sigma_{\theta r}) \,, \tag{11a}$$

$$(\nabla \cdot \boldsymbol{\sigma})_\phi \approx \partial_r \sigma_{\phi r} + \frac{1}{r_0}(\partial_\phi \sigma_{\phi\phi} + \partial_\theta \sigma_{\theta\phi}) \,, \tag{11b}$$

$$(\nabla \cdot \boldsymbol{\sigma})_\theta \approx \partial_r \sigma_{r\theta} + \frac{1}{r_0}(\partial_\phi \sigma_{\phi\theta} + \partial_\theta \sigma_{\theta\theta}) \,, \tag{11c}$$

$$\epsilon_{rr} \approx \partial_r u_r \,, \tag{11d}$$

$$\epsilon_{r\phi} \approx \frac{1}{2}\left(\partial_r u_\phi + \frac{1}{r_0}\partial_\phi u_r\right) \,, \tag{11e}$$

$$\epsilon_{r\theta} \approx \frac{1}{2}\left(\partial_r u_\theta + \frac{1}{r_0}\partial_\theta u_r\right) \,, \tag{11f}$$

$$\epsilon_{\phi\phi} \approx \frac{1}{r_0}\partial_\phi u_\phi \,, \tag{11g}$$

$$\epsilon_{\phi\theta} \approx \frac{1}{2r_0}(\partial_\phi u_\phi + \partial_\theta u_\phi) \,, \tag{11h}$$

$$\epsilon_{\theta\theta} \approx \frac{1}{r_0}\partial_\theta u_\theta \,. \tag{11i}$$

In order to derive expressions for the propagation speeds of pure SH and SV waves, we have to find plane wave solutions of equations (11a) to (11h). Strictly speaking this contradicts the assumption that our Earth model is finite and that we consider only a small volume of it. However, we can expect the resulting formulas to be physically reasonable if the spatial wavelength is small compared to the extensions of the small volume to which the wavefront is confined.

SV waves (radial polarisation): For a horizontally travelling wave with purely radial polarisation we have

$$u_\phi = u_\theta = 0 \,, \quad \partial_r = 0 \,, \tag{12}$$

and

$$\epsilon_{rr} = \epsilon_{\phi\phi} = \epsilon_{\phi\theta} = \epsilon_{\theta\theta} = 0\,. \tag{13}$$

The non-zero strain components are

$$\epsilon_{r\phi} = \frac{1}{2r_0}(\partial_\phi u_r)\,, \quad \epsilon_{r\theta} = \frac{1}{2r_0}(\partial_\theta u_r)\,. \tag{14}$$

For better readability, we replaced the $\approx$ sign by the $=$ sign in the above equations. Since we are interested only in the radial component of the displacement field, it suffices to consider the scalar equation

$$0 = \rho\partial_t^2 u_r - (\nabla\cdot\boldsymbol{\sigma})_r = \rho\partial_t^2 u_r - \frac{1}{r_0}(\partial_\phi\sigma_{r\phi} + \partial_\theta\sigma_{r\theta})\,. \tag{15}$$

Introducing the relations

$$\sigma_{r\phi} = 2(\mu+B)\epsilon_{r\phi} = \frac{1}{r_0}(\mu+B)\partial_\phi u_r\,, \tag{16}$$

$$\sigma_{r\theta} = 2(\mu+B)\epsilon_{r\theta} = \frac{1}{r_0}(\mu+B)\partial_\theta u_r\,, \tag{17}$$

into the wave equation (15) gives

$$0 = \rho\partial_t^2 u_r - \frac{(\mu+B)}{r_0^2}(\partial_\phi^2 u_r + \partial_\theta^2 u_r) \approx \rho\partial_t^2 u_r - (\mu+B)(\partial_y^2 u_r + \partial_z^2 u_r)\,. \tag{18}$$

With $u_x \approx u_r$ it follows that the propagation speed of SV waves is

$$c_{SV} = \sqrt{\frac{\mu+B}{\rho}}\,. \tag{19}$$

SH waves (horizontal polarisation): We assume that the propagation direction is $\mathbf{e}_\theta$ and that the polarisation direction is $\mathbf{e}_\phi$. This translates to

$$u_r = u_\theta = 0\,, \tag{20}$$

and

$$\partial_r = \partial_\phi = 0\,. \tag{21}$$

(Equivalently, one may choose $\mathbf{e}_\phi$ as propagation direction and $\mathbf{e}_\theta$ as polarisation direction. The resulting formula for the SH wave speed is the same because the medium is anisotropic with radial symmetry axis.) The only non-zero strain tensor component is

$$\epsilon_{\phi\theta} = \frac{1}{2r_0}\partial_\theta u_\phi\,. \tag{22}$$

Again, we wrote $=$ instead of $\approx$. It is implicit, that these are approximate relations only. The wave equation for the $\phi-$component of the displacement field is

$$0 = \rho\partial_t^2 u_\phi - (\nabla\cdot\boldsymbol{\sigma})_\phi = \rho\partial_t^2 u_\phi - \frac{1}{r_0}\partial_\theta\sigma_{\theta\phi}\,. \tag{23}$$

Substituting

$$\sigma_{\theta\phi} = 2\mu\epsilon_{\theta\phi} = \frac{\mu}{r_0}\partial_\theta u_\phi \tag{24}$$

into the wave equation (23) yields

$$0 = \rho\partial_t^2 u_\phi - \frac{\mu}{r_0}^2\partial_\theta^2 u_\phi \approx \rho\partial_t^2 - \mu\partial_z^2 u_y\,. \tag{25}$$

Hence, the SH wave speed is

$$c_{SH} = \sqrt{\frac{\mu}{\rho}}\,. \tag{26}$$

1.2.2 PH and PV waves in spherical coordinates

In an analysis similar to the one for SH and SV waves, one may consider P waves travelling in different coordinate directions. Here, we shall give the label PH to plane P waves travelling in horizontal direction, and the label PV to plane P waves travelling in radial direction. Again, the obtained formulas are approximations that are valid under the assumption that were discussed in the section on SH and SV waves.

PV waves: For a plane P wave travelling in radial direction we have

$$u_\phi = u_\theta = 0\,, \tag{27}$$

and

$$\partial_\phi = \partial_\theta = 0\,. \tag{28}$$

Following exactly the same steps outlined in the previous section gives the propagation speed of PV waves:

$$c_{PV} = \sqrt{\frac{\lambda + 2\mu}{\rho}}\,. \tag{29}$$

PH waves: Choosing $\mathbf{e}_\phi$ as propagation direction gives

$$u_r = u_\theta = 0\,, \tag{30}$$

and

$$\partial_\theta = \partial_r = 0\,. \tag{31}$$

As the resulting wave speed we find

$$c_{PH} = \sqrt{\frac{\lambda + 2\mu + A}{\rho}}\,. \tag{32}$$

Interestingly, the velocities of SH, SV, PH and PV waves specify only two of the three additional elastic parameters necessary for anisotropy with radial symmetry axis, namely A and B. Also radially propagating S waves do not allow us to find C, because they propagate with the velocity $\sqrt{(\mu + B)/\rho}$, just as SV waves. In fact, using plane waves, C can be determined only from P waves that do not travel in exactly radial or horizontal directions.

1.3 Anelasticity

The particular implementation of anelasticity is largely motivated by technical convenience and not so much by a deep understanding of seismic wave attenuation in the interior of the Earth. Even though significant progress has been made over the last years (e.g. Gung & Romanowicz, 2004), the time dependence of the elastic tensor components is only weakly constrained. Experimental studies have been made with materials that are likely to be abundant in the Earth's core and mantle, or with structural analogues (e.g. low-carbon iron alloys, Fo_{90} polycrystals, $CaTiO_3$). (See Jackson, 2000, for an excellent summary.) It was found that they can be reasonably represented by the Andrade model. If the stress is a Heaviside function, i.e., $\sigma(t) = H(t)$, then the strain response of the Andrade model is

$$J(t) = J_u + \beta t^n + t/\eta\,. \tag{33}$$

The function $J(t)$ is called strain relaxation function. Unfortunately, the Andrade model is hard to implement numerically. A more intuitive model that can be represented by a simple superposition of springs and dashpots is the Burgers model (e.g. Jackson, 2000). Its strain relaxation function is given by

$$J(t) = J_u + \delta J\left(1 - e^{-t/\tau}\right) + \frac{t}{\eta}\,, \tag{34}$$

For frequencies that are below 10 Hz, the Burgers model can fit the data as well as the Andrade model. If the period T of the elastic waves is significantly smaller than $\eta\delta J$, equation (34) may be simplified to

$$J(t) = J_u + \delta J\left(1 - e^{-t/\tau}\right)\,. \tag{35}$$

This is the strain relaxation function of a standard linear solid (e.g. Dahlen & Tromp, 1998). The above mentioned experiments usually considered a single mineral phase such as for example $CaTiO_3$. Since the Earth's mantle is composed of several mineral phases, we choose a superposition of standard linear solids. Our analysis roughly follows Robertsson et al. (1994).

It will be rather detailed in order to render the Fortran source code more easily understandable.
Assume that σ, c and ϵ are representative of some particular components of $\boldsymbol{\sigma}, \mathbf{C}$ and $\boldsymbol{\epsilon}$. Then a scalar version of the stress-strain relation (3) is given by

$$\partial_t \sigma(t) = (\dot{c} * \dot{\epsilon})(t) = \int_{-\infty}^{\infty} \dot{c}(t-t')\dot{\epsilon}(t')\, dt' \,. \tag{36}$$

The spatial dependence has been omitted for brevity. As already discussed, we choose the stress relaxation function c to be that of a superposition of N standard linear solids, i.e.,

$$c(t) := c_r \left[1 - \frac{1}{N} \sum_{p=1}^{N} \left(1 - \frac{\tau_{\epsilon p}}{\tau_{\sigma p}} \right) e^{-t/\tau_{\sigma p}} \right] H(t) \,, \tag{37}$$

where $\tau_{\epsilon p}$ and $\tau_{\sigma p}$ are the strain and stress relaxation times of the pth standard linear solid, respectively. The symbol H denotes the Heaviside function and c_r is the relaxed modulus. Equation (37) is still very general and different sets of relaxation times can give almost the same $c(t)$. Therefore, following the τ-method introduced by Blanch et al. (1995) we determine the $\tau_{\epsilon p}$ by defining a dimensionless variable τ through

$$\tau := \frac{\tau_{\epsilon p}}{\tau_{\sigma p}} - 1 \,. \tag{38}$$

This gives

$$c(t) = c_r \left[1 + \frac{\tau}{N} \sum_{p=1}^{N} e^{-t/\tau_{\sigma p}} \right] H(t) \,. \tag{39}$$

Differentiating (39) and introducing the result into (36) yields

$$\partial_t \sigma(t) = c_r (1+\tau)\, \dot{\epsilon}(t) + \sum_{p=1}^{N} M_p \,, \tag{40}$$

where the memory variables M_p are defined by

$$M_p := -\frac{\tau c_r}{N \tau_{\sigma p}} \int_{-\infty}^{\infty} e^{-(t-t')/\tau_{\sigma p}}\, H(t-t')\, \dot{\epsilon}(t')\, dt' \,. \tag{41}$$

The differentiation of (41) with respect to time yields a set of simple first-order differential equations for the memory variables:

$$\partial_t M_p = -\frac{\tau c_r}{N \tau_{\sigma p}}\, \dot{\epsilon} - \frac{1}{\tau_{\sigma p}}\, M_p \,. \tag{42}$$

Hence, anelasticity can be modelled by solving differential equations for the memory variables simultaneously with the momentum equation (1) and the stress-strain relation (3, 40).

Based on the previous analysis we can now give an explicit version of equation (3):

$$\partial_t \sigma_{rr} = \lambda_r (1+\tau_\lambda)\,(\dot\epsilon_{rr} + \dot\epsilon_{\varphi\varphi} + \dot\epsilon_{\theta\theta}) + 2\mu_r (1+\tau_\mu)\,\dot\epsilon_{rr} + C\,(\dot\epsilon_{\varphi\varphi} + \dot\epsilon_{\theta\theta}) + \sum_{p=1}^{N} \left(L_p^{rr} + L_p^{\varphi\varphi} + L_p^{\theta\theta} + 2M_p^{rr} \right) , \tag{43a}$$

$$\partial_t \sigma_{\varphi\varphi} = \lambda_r (1+\tau_\lambda)\,(\dot\epsilon_{rr} + \dot\epsilon_{\varphi\varphi} + \dot\epsilon_{\theta\theta}) + 2\mu_r (1+\tau_\mu)\,\dot\epsilon_{\varphi\varphi} + C\,\dot\epsilon_{rr} + A\,(\dot\epsilon_{\varphi\varphi} + \dot\epsilon_{\theta\theta}) + \sum_{p=1}^{N} \left(L_p^{rr} + L_p^{\varphi\varphi} + L_p^{\theta\theta} + 2M_p^{\varphi\varphi} \right) , \tag{43b}$$

$$\partial_t \sigma_{\theta\theta} = \lambda_r (1+\tau_\lambda)\,(\dot\epsilon_{rr} + \dot\epsilon_{\varphi\varphi} + \dot\epsilon_{\theta\theta}) + 2\mu_r (1+\tau_\mu)\,\dot\epsilon_{\theta\theta} + C\,\dot\epsilon_{rr} + A\,(\dot\epsilon_{\varphi\varphi} + \dot\epsilon_{\theta\theta}) + \sum_{p=1}^{N} \left(L_p^{rr} + L_p^{\varphi\varphi} + L_p^{\theta\theta} + 2M_p^{\theta\theta} \right) , \tag{43c}$$

$$\partial_t \sigma_{r\varphi} = 2\mu_r (1+\tau_\mu)\,\dot\epsilon_{r\varphi} + 2B\dot\epsilon_{r\varphi} + 2\sum_{p=1}^{N} M_p^{r\varphi} , \tag{43d}$$

$$\partial_t \sigma_{r\theta} = 2\mu_r (1+\tau_\mu)\,\dot\epsilon_{r\theta} + 2B\dot\epsilon_{r\theta} + 2\sum_{p=1}^{N} M_p^{r\theta} , \tag{43e}$$

$$\partial_t \sigma_{\varphi\theta} = 2\mu_r (1+\tau_\mu)\,\dot\epsilon_{\varphi\theta} + 2\sum_{p=1}^{N} M_p^{\varphi\theta} . \tag{43f}$$

The time evolution of the memory variables is determined through the following set of differential equations:

$$\partial_t M_p^{ij} = -\frac{\mu_r \tau_\mu}{N \tau_{\sigma p}^{\mu}}\,\dot\epsilon_{ij} - \frac{1}{\tau_{\sigma_{\sigma p}^{\mu}}} M_p^{ij} , \tag{44a}$$

$$\partial_t L_p^{ij} = -\frac{\lambda_r \tau_\lambda}{N \tau_{\sigma p}^{\lambda}}\,\dot\epsilon_{ij} - \frac{1}{\tau_{\sigma p}^{\lambda}} L_p^{ij} . \tag{44b}$$

Note that we do not implement anelasticity for the anisotropy parameters A, B and C.

In seismology there has traditionally been more emphasis on the quality factor Q than on particular stress or strain relaxation functions. The exact definition of Q is based on the definition of the complex modulus:

$$c(\nu) := \mathbf{i}\,\nu \int_0^\infty c(t)\, e^{-\mathbf{i}\nu t}\, dt , \tag{45}$$

with $\nu := \omega + \mathbf{i}\gamma$. Then

$$Q(\omega) := \frac{\mathrm{Re}(c(\omega))}{\mathrm{Im}(c(\omega))} . \tag{46}$$

If $\mathrm{Im}(c(\omega)) \ll \mathrm{Re}(c(\omega))$, Q can be interpreted in terms of the maximum elastic energy E_{max} and the energy that is dissipated per cycle, E_{diss}:

$$E_{diss}/E_{max} = 4\pi Q^{-1} . \tag{47}$$

For our stress relaxation function defined in equation (39) we find

$$Q(\omega) = \frac{\sum_{p=1}^{N} \left(1 + \frac{\omega^2 \tau_{\sigma p}^2 \tau}{1+\omega^2 \tau_{\sigma p}^2} \right)}{\sum_{p=1}^{N} \left(\frac{\omega \tau_{\sigma p} \tau}{1+\omega^2 \tau_{\sigma p}^2} \right)} . \tag{48}$$

An early analysis of seismic wave attenuation was carried out by Born (1941). It follows from his laboratory studies that Q is frequency independent in dry sedimentary rocks, meaning that the elastic energy loss can be attributed to solid friction. Born also found that a strong frequency dependence of Q results from the inclusion of even small amounts of water and he noted that the extrapolation of the solid friction behaviour to greater depths is "admittedly speculation." Still, a constant Q has become the standard in seismology. Blanch et al. (1995) gave a simple algorithm that allows to construct a constant Q from equation (48). In recent years it has become more and more evident that Q in the Earth's mantle is not

constant, but proportional to ω^α, with α ranging between 0.2 and 0.4 (e.g. Romanowicz & Durek, 2000; Cheng & Kennett, 2002; Shito et al., 2004). We therefore included a Matlab file called `relaxation_times.m` in the `fd3s` package, which determines the parameters τ and $\tau_{\sigma p}$ in equation (48) for an arbitrary $Q(\omega)$. The algorithm minimises the L_2 distance between equation (48) and the prescribed frequency dependence of Q with a simple Simulated Annealing technique (Kirkpatrick et al, 1983).

2 Discretisation

2.1 Discretisation in space

In order to solve equations (1, 6a-6c, 7a-7f), they have to be discretised in both time and space. The principal ideas of the scheme that we adopted can be found in Virieux (1984). We choose a constant grid spacing, with increments $\Delta r, \Delta\varphi$ and $\Delta\theta$ in the r, φ, and θ directions, respectively. The continuous fields are replaced by their discrete versions - indicated by a bar - as follows:

$$\epsilon_{nn}(r,\varphi,\theta) \to \bar{\epsilon}_{nn}(i,j,k) = \bar{\epsilon}_{nn}|_{ijk}\,, \tag{49a}$$
$$\epsilon_{r\varphi}(r-\Delta r/2,\varphi+\Delta\varphi/2,\theta) \to \bar{\epsilon}_{r\varphi}(i,j,k) = \bar{\epsilon}_{r\varphi}|_{ijk}\,, \tag{49b}$$
$$\epsilon_{r\theta}(r-\Delta r/2,\varphi,\theta+\Delta\theta/2) \to \bar{\epsilon}_{r\theta}(i,j,k) = \bar{\epsilon}_{r\theta}|_{ijk}\,, \tag{49c}$$
$$\epsilon_{\varphi\theta}(r,\varphi+\Delta\varphi/2,\theta+\Delta\theta/2) \to \bar{\epsilon}_{\varphi\theta}(i,j,k) = \bar{\epsilon}_{\varphi\theta}|_{ijk}\,, \tag{49d}$$

$$\sigma_{nn}(r,\varphi,\theta) \to \bar{\sigma}_{nn}(i,j,k) = \bar{\sigma}_{nn}|_{ijk}\,, \tag{49e}$$
$$\sigma_{r\varphi}(r-\Delta r/2,\varphi+\Delta\varphi/2,\theta) \to \bar{\sigma}_{r\varphi}(i,j,k) = \bar{\sigma}_{r\varphi}|_{ijk}\,, \tag{49f}$$
$$\sigma_{r\theta}(r-\Delta r/2,\varphi,\theta+\Delta\theta/2) \to \bar{\sigma}_{r\theta}(i,j,k) = \bar{\sigma}_{r\theta}|_{ijk}\,, \tag{49g}$$
$$\sigma_{\varphi\theta}(r,\varphi+\Delta\varphi/2,\theta+\Delta\theta/2) \to \bar{\sigma}_{\varphi\theta}(i,j,k) = \bar{\sigma}_{\varphi\theta}|_{ijk}\,, \tag{49h}$$

$$v_r(r-\Delta r/2,\varphi,\theta) \to \bar{v}_r(i,j,k) = \bar{v}_{ijk}\,, \tag{49i}$$
$$v_\varphi(r,\varphi+\Delta\varphi/2,\theta) \to \bar{v}_\varphi(i,j,k) = \bar{v}_\varphi|_{ijk}\,, \tag{49j}$$
$$v_\theta(r,\varphi,\theta+\Delta\theta/2) \to \bar{v}_\theta(i,j,k) = \bar{v}_\theta|_{ijk}\,. \tag{49k}$$

The spatial derivatives are approximated by fourth-order finite differences. For example

$$\begin{aligned}
\partial_\varphi\sigma_{\varphi\varphi}(r,\varphi+\Delta\varphi/2,\theta) \;\to\; & \frac{9}{8\Delta\varphi}[\sigma_{rr}(r,\varphi+\Delta\varphi,\theta)-\sigma_{rr}(r,\varphi,\theta)] \\
& -\frac{1}{24\Delta\varphi}[\sigma_{rr}(r,\varphi+2\Delta\varphi,\theta)-\sigma_{rr}(r,\varphi-\Delta\varphi,\theta)] \\
\to\; & \frac{9}{8\Delta\varphi}[\bar{\sigma}_{rr}(i,j+1,k)-\bar{\sigma}_{rr}(i,j,k)] \\
& -\frac{1}{24\Delta\varphi}[\bar{\sigma}_{rr}(i,j+2,k)-\bar{\sigma}_{rr}(i,j-1,k)] =: \partial_\varphi\bar{\sigma}_{\varphi\varphi}(i,j,k)\,.
\end{aligned} \tag{50}$$

Evidently, the discrete fields and their respective discrete derivatives are now located at different points, even though they have the same index (figure (2)). This has the advantage that the grid spacing is effectively reduced and that the method converges faster. However, equations (6a) to (7f) occasionally require knowledge of a field and its derivative at the same location, and therefore interpolation becomes necessary. Note that this inconsistency of the staggered grid does not exist in cartesian coordinates (e.g. Igel et al., 1995). Interpolations are also necessary for the elastic parameters. They are usually defined at (r,φ,θ), i.e., at the same locations as the diagonal stress and strain rate components.

2.2 Discretisation in time

The discretisation in time is implemented as a second-order finite-difference approximation. This creates an explicit scheme that allows us to step forward in time without solving a large matrix equation. We start with a forward step of the velocity field:

$$\begin{aligned}
\bar{\mathbf{v}}(t+\Delta t) &= \bar{\mathbf{v}}(t) + \Delta t\,\partial_t\bar{\mathbf{v}}(t+\Delta t/2) \\
&= \bar{\mathbf{v}}(t) + \Delta t\left[\frac{1}{\rho}\nabla\cdot\bar{\boldsymbol{\sigma}}(t+\Delta t/2) + \frac{1}{\rho}\bar{\mathbf{f}}(t+\Delta t/2)\right].
\end{aligned} \tag{51}$$

The spatial dependence of the field variables has been omitted for brevity. A discrete version of $\nabla\cdot\boldsymbol{\sigma}$ can be obtained from equations (6a) to (6c). Once $\bar{\mathbf{v}}(t+\Delta t)$ has been computed from equation (51), the discretised strain rate tensor $\dot{\bar{\boldsymbol{\epsilon}}}$ at the time $t+\Delta t$ can be calculated from equations (7a) to (7f). It therefore becomes possible to propagate the stress field forward in

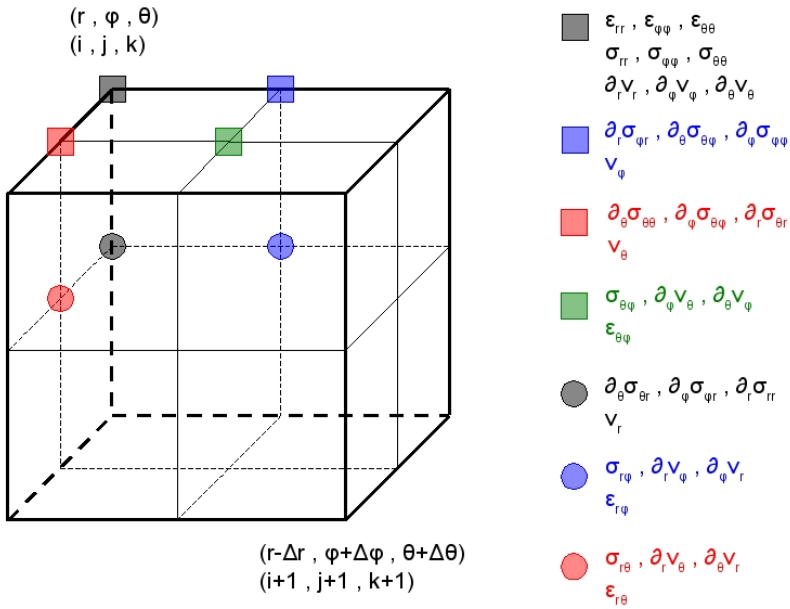

Figure 2: Staggered grid scheme: Locations of the field variables with multi-index (i, j, k). Note that the index i increases with decreasing radius and increasing depth.

time:

$$\begin{aligned}\bar{\boldsymbol{\sigma}}(t+3\Delta t/2) &= \bar{\boldsymbol{\sigma}}(t+\Delta t/2) + \Delta t\,\partial_t\bar{\boldsymbol{\sigma}}(t+\Delta t)\\ &= \bar{\boldsymbol{\sigma}}(t+\Delta t/2) + \Delta t\left[\int_{-\infty}^{\infty}\dot{\mathbf{C}}(t'):\dot{\bar{\boldsymbol{\epsilon}}}(t+\Delta t-t')\,dt'\right]. \qquad (52)\end{aligned}$$

The convolution on the right-hand side of (52) is explicitly given by the equations (43a) to (43f). It remains to consider the memory variables L_p^{ij} and M_p^{ij}. Just as $\partial_t\bar{\boldsymbol{\sigma}}$ and $\dot{\bar{\boldsymbol{\epsilon}}}$ they have to be known at times $t+\Delta t$. Since the differential equations for L_p^{ij} and M_p^{ij} involve both the memory variables themselves and their time derivatives, it is not possible to use a second-order approximation without saving all memory variables and the strain rate tensor for at least one previous time step. Since this would substantially increase both the memory requirements and the computing time, we adopt a simple first order scheme for the memory variables:

$$\begin{aligned}\bar{M}_p^{ij}(t+\Delta t) &= \bar{M}_p^{ij}(t) + \Delta t\,\partial_t\bar{M}_p^{ij}(t)\\ &= \bar{M}_p^{ij}(t) - \Delta t\left[\frac{\mu_r\tau_\mu}{N\tau_{\sigma p}^{\mu}}\,\dot{\bar{\epsilon}}_{ij}(t) + \frac{1}{\tau_{\sigma_{\sigma p}^{\mu}}}\bar{M}_p^{ij}(t)\right], \qquad (53)\\ \bar{L}_p^{ij}(t+\Delta t) &= \bar{L}_p^{ij}(t) + \Delta t\,\partial_t\bar{L}_p^{ij}(t)\\ &= \bar{L}_p^{ij}(t) - \Delta t\left[\frac{\lambda_r\tau_\lambda}{N\tau_{\sigma p}^{\lambda}}\,\dot{\bar{\epsilon}}_{ij}(t) + \frac{1}{\tau_{\sigma_{\sigma p}^{\lambda}}}\bar{L}_p^{ij}(t)\right], \qquad (54)\end{aligned}$$

In order to initialise the time stepping, the fields $\bar{\mathbf{v}}(0)$ and $\bar{\boldsymbol{\sigma}}(\Delta t/2)$ must be known. Since there is no equation that allows us to compute $\bar{\boldsymbol{\sigma}}(\Delta t/2)$, we simply set $\bar{\boldsymbol{\sigma}}(\Delta t/2)$ equal to the true initial value $\bar{\boldsymbol{\sigma}}(0)$.

2.3 The free surface

The numerical treatment of the free surface requires special attention because it does not follow directly from the discretisation in the interior of the spherical section. In this sense, the finite difference approach is not holistic.

The staggered grid scheme (figure 2) implies that the computations of the discrete versions of $\nabla\mathbf{v}$ and $\nabla\cdot\boldsymbol{\sigma}$ require grid points above the free surface:

$$\bar{\sigma}_{r\theta}|_{-1jk}\,,\bar{\sigma}_{r\theta}|_{-2jk} \;\rightarrow\; \partial_r\bar{\sigma}_{r\theta}|_{0jk}\,, \tag{55a}$$
$$\bar{\sigma}_{r\varphi}|_{-1jk}\,,\bar{\sigma}_{r\varphi}|_{-2jk} \;\rightarrow\; \partial_r\bar{\sigma}_{r\varphi}|_{0jk}\,, \tag{55b}$$
$$\bar{\sigma}_{rr}|_{-1jk} \;\rightarrow\; \partial_r\bar{\sigma}_{rr}|_{0jk}\,, \tag{55c}$$
$$\bar{v}_{\theta}|_{-1jk} \;\rightarrow\; \partial_r\bar{v}_{\theta}|_{0jk}\,, \tag{55d}$$
$$\bar{v}_{\varphi}|_{-1jk} \;\rightarrow\; \partial_r\bar{v}_{\varphi}|_{0jk}\,, \tag{55e}$$
$$\bar{v}_{r}|_{-1jk}\,,\bar{v}_{r}|_{-2jk} \;\rightarrow\; \partial_r\bar{v}_{r}|_{0jk}\,. \tag{55f}$$

The values above the free surface are initially unavailable. Therefore, they have to be calculated explicitly from the free surface boundary conditions

$$\sigma_{rr}|_{r=R} = 0\,, \tag{56a}$$
$$\sigma_{r\varphi}|_{r=R} = 0\,, \tag{56b}$$
$$\sigma_{r\theta}|_{r=R} = 0\,. \tag{56c}$$

Equation (56a) can be discretised directly because $\bar{\sigma}_{rr}|_{0jk}$ is defined at the surface:

$$\bar{\sigma}_{rr}|_{0jk} = 0\,. \tag{57a}$$

The value of $\bar{\sigma}_{rr}$ one grid point above the free surface may be obtained via an anti-symmetry relation:

$$\bar{\sigma}_{rr}|_{-1jk} = -\bar{\sigma}_{rr}|_{1jk}\,. \tag{57b}$$

The discrete stress tensor components $\bar{\sigma}_{r\theta}$ and $\bar{\sigma}_{r\varphi}$ are not defined directly at the surface. We therefore treat them with similar anti-symmetry relations that force at least the linearly interpolated solutions to zero:

$$\bar{\sigma}_{r\theta}|_{-1jk} = -\bar{\sigma}_{r\theta}|_{0jk}\,, \quad \bar{\sigma}_{r\theta}|_{-2jk} = -\bar{\sigma}_{r\theta}|_{1jk}\,, \tag{57c}$$
$$\bar{\sigma}_{r\varphi}|_{-1jk} = -\bar{\sigma}_{r\varphi}|_{0jk}\,, \quad \bar{\sigma}_{r\varphi}|_{-2jk} = -\bar{\sigma}_{r\varphi}|_{1jk}\,. \tag{57d}$$

The values of $\bar{\mathbf{v}}$ above the surface can be obtained through the stress strain relation. Its continuous version is

$$\partial_t\sigma_{rr} = (\tilde{\lambda}+2\tilde{\mu})\,\partial_r v_r + \frac{(\tilde{\lambda}+C)}{r}\left[\frac{1}{\sin\theta}\,\partial_\varphi v_\varphi + 2v_r + v_\theta\cot\theta + \partial_\theta v_\theta\right] + \sum_{p=1}^{N}\left(L_p^{rr} + L_p^{\varphi\varphi} + L_p^{\theta\theta} + 2M_p^{rr}\right) \tag{58a}$$

$$\partial_t\sigma_{r\varphi} = (\tilde{\mu}+B)\left[\partial_r v_\varphi + \frac{1}{r\,\sin\theta}\,\partial_\varphi v_r - \frac{1}{r}\,v_\varphi\right] + 2\sum_{p=1}^{N} M_p^{r\varphi}\,, \tag{58b}$$

$$\partial_t\sigma_{r\theta} = (\tilde{\mu}+B)\left[\partial_r v_\theta + \frac{1}{r}\,\partial_\theta v_r - \frac{1}{r}\,v_\theta\right] + 2\sum_{p=1}^{N} M_p^{r\theta}\,. \tag{58c}$$

Equation (56a) implies

$$0 = (\tilde{\lambda}+2\tilde{\mu})\,\partial_r v_r\Big|_{r=R} + \frac{(\tilde{\lambda}+C)}{r}\left[\frac{1}{\sin\theta}\,\partial_\varphi v_\varphi + 2v_r + v_\theta\cot\theta + \partial_\theta v_\theta\right]\Bigg|_{r=R} + \sum_{p=1}^{N}\left(L_p^{rr} + L_p^{\varphi\varphi} + L_p^{\theta\theta} + 2M_p^{rr}\right)\Bigg|_{r=R}\,. \tag{59}$$

This equation can not be discretised directly, because $\bar{v}_r$ and $\bar{v}_\theta$ are not defined at the adequate grid point. Therefore, we use the horizontally interpolated values of $\bar{v}_\theta$, denoted by

$\bar{\bar{v}}_\theta$. Moreover, we replace $\bar{v}_r|_{0jk}$ by the vertically interpolated values $\frac{1}{2}\left(\bar{v}_r|_{0jk} + \bar{v}_r|_{-1jk}\right)$. Introducing these approximations into (59) yields

$$0 = (\tilde{\lambda} + 2\tilde{\mu})\, \partial_r \bar{v}_r|_{0jk} + \frac{(\tilde{\lambda} + C)}{r} \left[\frac{1}{\sin\theta}\, \partial_\varphi \bar{v}_\varphi + v_r + \partial_\theta \bar{v}_\theta + \bar{\bar{v}}_\theta \cot\theta\right]\Bigg|_{0jk}$$
$$+ \frac{(\tilde{\lambda} + C)}{r}\, \bar{v}_r\Bigg|_{-1jk} + \sum_{p=1}^{N} \left(\bar{L}_p^{rr} + \bar{L}_p^{\varphi\varphi} + \bar{L}_p^{\theta\theta} + 2\bar{M}_p^{rr}\right)\Bigg|_{0jk} \tag{60}$$

In order to obtain $\bar{v}_r|_{-1jk}$, we set

$$\partial_r \bar{v}_r|_{0jk} \doteq \frac{1}{\Delta r}\left[\bar{v}_r|_{-1jk} - \bar{v}_r|_{0jk}\right] . \tag{61}$$

This second-order approximation is obviously motivated by pure mathematical convenience. Even though it is practical, the order of the finite difference scheme is reduced to 2, at least at the surface. Regarding equation (61), remember that the radial index increases with decreasing radius. Finally, introducing (61) into (60) gives

$$\bar{v}_r|_{-1jk} = \frac{R_2}{R_1}\, \bar{v}_r|_{0jk} + \frac{R_3}{R_1}\left[\frac{1}{\sin\theta}\, \partial_\varphi \bar{v}_\varphi + \bar{v}_r + \partial_\theta \bar{v}_\theta + \bar{\bar{v}}_\theta \cot\theta\right]\Bigg|_{0jk}$$
$$- \frac{1}{R_1} \sum_{p=1}^{N} \left(\bar{L}_p^{rr} + \bar{L}_p^{\varphi\varphi} + \bar{L}_p^{\theta\theta} + 2\bar{M}_p^{rr}\right)\Bigg|_{0jk} , \tag{62a}$$

with

$$R_1 := \left[\frac{(\tilde{\lambda} + 2\tilde{\mu})}{\Delta r} + \frac{(\tilde{\lambda} + C)}{r}\right]\Bigg|_{-1jk} , \tag{62b}$$

$$R_2 := \frac{(\tilde{\lambda} + 2\tilde{\mu}}{\Delta r}\Bigg|_{0jk} , \tag{62c}$$

$$R_3 := -\frac{(\tilde{\lambda} - C)}{r}\Bigg|_{0jk} . \tag{62d}$$

Now that $\bar{v}_r|_{-1jk}$ has been found, we apply the anti-symmetry relations (57c) and (57d):

$$-(\tilde{\mu} + B)\left[\partial_r \bar{v}_\varphi + \frac{1}{r\,\sin\theta}\, \partial_\varphi \bar{v}_r - \frac{1}{r}\, \bar{\bar{v}}_\varphi\right]\Bigg|_{0jk} - 2\sum_{p=1}^{N} \bar{M}_p^{r\varphi}\big|_{0jk}$$
$$= (\tilde{\mu} + B)\left[\partial_r \bar{v}_\varphi + \frac{1}{r\,\sin\theta}\, \partial_\varphi \bar{v}_r - \frac{1}{r}\, \bar{\bar{v}}_\varphi\right]\Bigg|_{-1jk} + 2\sum_{p=1}^{N} \bar{M}_p^{r\varphi}\big|_{-1jk} , \tag{63}$$

and

$$-(\tilde{\mu} + B)\left[\partial_r \bar{v}_\theta + \frac{1}{r}\, \partial_\theta \bar{v}_r - \frac{1}{r}\, \bar{\bar{v}}_\theta\right]\Bigg|_{0jk} - 2\sum_{p=1}^{N} \bar{M}_p^{r\theta}\Big|_{0jk}$$
$$= (\tilde{\mu} + B)\left[\partial_r \bar{v}_\theta + \frac{1}{r}\, \partial_\theta \bar{v}_r - \frac{1}{r}\, \bar{\bar{v}}_\theta\right]\Bigg|_{-1jk} + 2\sum_{p=1}^{N} \bar{M}_p^{r\theta}\Big|_{-1jk} \tag{64}$$

Again, $\bar{v}_\varphi$ and $\bar{v}_\theta$ had to be interpolated:

$$\bar{\bar{v}}_\varphi|_{-1jk} := \frac{1}{2}[\bar{v}_\varphi|_{-1jk} + \bar{v}_\varphi|_{0jk}] , \tag{65a}$$

$$\bar{\bar{v}}_\varphi|_{0jk} := \frac{1}{2}[\bar{v}_\varphi|_{0jk} + \bar{v}_\varphi|_{1jk}] , \tag{65b}$$

$$\bar{\bar{v}}_\theta|_{-1jk} := \frac{1}{2}[\bar{v}_\theta|_{-1jk} + \bar{v}_\theta|_{0jk}] , \tag{65c}$$

$$\bar{\bar{v}}_\theta|_{0jk} := \frac{1}{2}[\bar{v}_\theta|_{0jk} + \bar{v}_\theta|_{1jk}] . \tag{65d}$$

Since the finite difference scheme is already reduced to second order at the surface, we employ the following approximations:

$$\partial_r \bar{v}_\varphi|_{-1jk} \doteq \frac{1}{\Delta r}\left[\bar{v}_\varphi|_{-1jk} - \bar{v}_\varphi|_{0jk}\right] , \tag{66a}$$

$$\partial_r \bar{v}_\varphi|_{0jk} \doteq \frac{1}{\Delta r}\left[\bar{v}_\varphi|_{0jk} - \bar{v}_\varphi|_{1jk}\right] , \tag{66b}$$

$$\partial_r \bar{v}_\theta|_{-1jk} \doteq \frac{1}{\Delta r}\left[\bar{v}_\theta|_{-1jk} - \bar{v}_\theta|_{0jk}\right] , \tag{66c}$$

$$\partial_r \bar{v}_\theta|_{0jk} \doteq \frac{1}{\Delta r}\left[\bar{v}_\theta|_{0jk} - \bar{v}_\theta|_{1jk}\right] . \tag{66d}$$

Combining equations (63) to (66d), gives - after some tedious algebraic manipulations - the following expressions for $\bar{v}_\varphi|_{-1jk}$ and $\bar{v}_\theta|_{1-jk}$.

$$\begin{aligned}\bar{v}_\varphi|_{-1jk} = {} & \frac{1}{A_1}\left(\frac{1}{r}\,\bar{v}_\varphi - \frac{1}{\sin\theta}\,\partial_\varphi \bar{v}_r\right)\Big|_{0jk} - \frac{1}{A_1}\left(\frac{1}{r\,\sin\theta}\partial_\varphi \bar{v}_r\right)\Big|_{-1jk} \\ & + \frac{A_2}{A_1}\,\bar{v}_\varphi|_{1jk} - \frac{4}{A_1(\tilde{\mu}+B)}\sum_{p=1}^{N} M_p^{r\varphi}\big|_{0jk} ,\end{aligned} \tag{67}$$

$$\begin{aligned}\bar{v}_\theta|_{-1jk} = {} & \frac{1}{A_1}\left(\frac{1}{r}\bar{v}_\theta - \frac{1}{r}\,\partial_\theta\,\bar{v}_r\right)\Big|_{0jk} - \frac{1}{A_1}\left(\frac{1}{r}\,\partial_\theta \bar{v}_r\right)\Big|_{-1jk} \\ & + \frac{A_2}{A_1}\,\bar{v}_\theta|_{1jk} - \frac{4}{A_1(\tilde{\mu}+B)}\sum_{p=1}^{N} M_p^{r\theta}\Big|_{0jk} .\end{aligned} \tag{68}$$

The scalars A_1 and A_2 are defined as

$$A_1 := \left(\frac{1}{\Delta r} - \frac{1}{2r}\right)\Big|_{-1jk} = \left(\frac{1}{\Delta r} - \frac{1}{2(R+\Delta r)}\right) , \tag{69a}$$

$$A_2 := \left(\frac{1}{\Delta r} + \frac{1}{2r}\right)\Big|_{1jk} = \left(\frac{1}{\Delta r} + \frac{1}{2(R-\Delta r)}\right) . \tag{69b}$$

Note that for deriving equations (67) and (68) we have assumed that $\bar{M}_p^{r\varphi}|_{-1jk}$ and $\bar{M}_p^{r\theta}|_{-1jk}$ are approximately equal to $\bar{M}_p^{r\varphi}|_{0jk}$ and $\bar{M}_p^{r\theta}|_{0jk}$, respectively. Not doing so would require us to find and solve equations for the memory variables above the surface. This however seems to be an unnecessary effort.

2.4 Absorbing boundaries

`fd3s` restricts the spatial domain in which the discretised equations of motion are solved to a spherical section. From a purely mathematical point of view, this domain has to exclude the centre of the sphere ($r = 0$) in order to avoid singularities in equations (6a) to (6c) and (7a) to (7f). As we shall see later, stability requirements force us to exclude the polar regions as well, because the volume of a grid cell tends to zero as θ approaches 0 or π. Another argument for the limitation of the spatial domain is of course the minimisation of the computational costs. The introduction of unphysical boundaries automatically results in unphysical reflections, unless they are suppressed by absorbing boundary conditions. An efficient implementation of absorbing boundary conditions has been proposed by Cerjan et al. (1985): After each time step the discrete fields $\bar{\mathbf{v}}$ and $\bar{\boldsymbol{\sigma}}$ near the boundaries are multiplied by a Gaussian damping function defined as

$$G(i) = \exp\left[-\left(\frac{N-i}{\alpha}\right)\right] , \tag{70}$$

where N is the width of the damping region in grid points and i is the distance to the boundary. Outside the damping region, i.e., for $i > N$, all fields remain unchanged. Nissen-Meyer (2001) found that $N = 40$ and $\alpha = 3N$ is sufficient to eliminate unphysical reflections.

3 Implementation and technical details

The finite difference scheme described so far, has been implemented in the form of a `fortran90` program called `fd3s`. Some of the technical details concerning this implementation will be outlined in this section. For greater generality, the focus will be on the parallel version of `fd3s`. Running the program on one single processor only is straightforward and merely requires the specification of three simple input parameters.

3.1 Directory structure

All necessary files are contained in the directory `FD3S` and its subdirectories `DATA`, `MODELS` and `MATLAB`.

In addition to the source code which will be described later, the directory `FD3S` contains the `Par` file including the most important input parameters such as the model size, source location and source type.
The directory `MATLAB` contains a collection of useful and simple Matlab tools that help to generate input and visualise the output. Detailed explanations are provided in the headers of the different M-files and will therefore not be repeated here.
All input files defining the physical model can be found in the directory `MODELS`. Among them are the distributions of inverse density and elastic parameters, as well as the initial displacement and stress fields.
`DATA` comprises three subdirectories named `COORDINATES`, `LOGFILES` and `OUTPUT`. During the initialisation phase each processor writes the coordinates of its part of the entire model into `COORDINATES`. Similarly, logfiles for each processor are written to `LOGFILES`. The generated seismograms and wavefield snapshots can be found in `OUTPUT`.

3.2 Source code

The `fd3s` source code is composed of 8 `fortran90` files that have to be compiled together. A brief description of their contents will be given in the following paragraphs.

1. `fd3s_main.f90` is the principal source file. It comprises calls to subroutines that initialise `fd3s`, read the input files and write the output. Moreover, `fd3s_main.f90` includes the time stepping loop.

2. `fd3s_modules.f90` includes two `fortran90` modules called `parameters` and `variables`. Since dynamic memory allocation is still problematic in `fortran90`, maximum field sizes are specified in `parameters`. Especially for the purpose of efficient parallel computing it is important to keep the parameters `nx`, `ny` and `nz` as small as possible. They give the maximum fields sizes for each processor in θ, ϕ and r direction, respectively. Note that these are not the maximum field sizes for the entire model but for the different parts of the model assigned to their respective processes.
   Global variables are declared in `variables`. Even though their meaning is given in the form of comments, the most important ones will be listed here:

$$\texttt{*x} = *_\theta\,, \quad \texttt{*y} = *_\phi\,, \quad \texttt{*z} = *_r\,,$$
$$\texttt{w11} = v_\theta\,, \quad \texttt{w12} = v_\varphi\,, \quad \texttt{w13} = v_r\,,$$
$$\texttt{w14} = \sigma_{\theta\theta}\,, \quad \texttt{w15} = \sigma_{\varphi\varphi}\,, \quad \texttt{w16} = \sigma_{rr}\,,$$
$$\texttt{w17} = \sigma_{\theta\varphi}\,, \quad \texttt{w18} = \sigma_{\theta r}\,, \quad \texttt{w19} = \sigma_{\varphi r}\,.$$

3. `fd3s_init.f90` initialises the coordinate axes for the different processors as well as the parameters necessary for the linear receiver interpolation. In addition to this, the two-dimensional fields necessary for the free surface implementation are initialised in `fd3s_init.f90`.

4. `fd3s_input.f90` first reads input parameters from the files `Par` and `boxfile` and distributes them among the different processes. (The `boxfile` will be explained in the subsection on parallelisation.) Subsequently, each process reads the following input from the directory `MODELS`: distributions of inverse density, elastic parameters and relaxation times, initial velocity and stress distributions. The initial values become unnecessary and are automatically assumed to be zero, if the parameter `is_homogeneous` in the `Par` file is set to 1.

5. `fd3s_evolution.f90` performs one forward time step of the stress and velocity fields. The subroutine `fd3s_evolution` starts with the communication of stress fields between different processes. This will later be described in detail. After all processes received the relevant stress fields, the stress divergence can be computed, which then allows to extrapolate the velocity field. The updated velocity field is then also communicated between the processors. This is followed by the computation of the strain rate tensor and the application of Hooke's relation. Finally, the stress field is updated. Depending on whether the medium is dissipative or not, `fd3s_evolution` also performs the time stepping of the memory variables.
   The subroutine `fs_graves`, also contained in `fd3s_evolution.f90`, is responsible for the computation of the velocity values above the surface, which are necessary for the implementation of the free surface. Another subroutine in `fd3s_evolution.f90`, called `pder2`, computes spatial derivatives of two-dimensional fields. This is also used for the free surface implementation.
6. `fd3s_oper.f90` contains the subroutines `inter` and `pder`, used for spatial interpolation and differentiation, respectively.
7. `fd3s_comm_tap.f90` includes the subroutine `comm_tap_v` which is responsible for the exchange of velocity fields between the boundary regions of different processors and for the implementation of the absorbing boundaries. The subroutine `comm_tap_s` performs exactly the same tasks for the stress fields. Both subroutines are essentially the same. Depending on the rank of a process, the velocity and stress fields in the boundary regions of the process' part of the model are either sent to other processes or damped.
8. `fd3s_output.f90` is composed of the subroutines `fd3s_output` and `record_seismograms`. After each time step, `record_seismograms` writes the new velocity values at the receiver locations into an array which can be written to a file using `fd3s_output`. In addition to this, `fd3s_output` also writes the velocity snapshots into files located in the directory `OUTPUT`.

3.3 Input files

Most of the input files are contained in the directory `MODELS`. There are four types of input, namely initial values, material parameters, receiver locations and the source time function.

Initial values for the stress and velocity fields can most conveniently be generated using the `fortran90` programme `generate_initial`, the source code of which is also included in the directory `MODELS`. It can be modified in order to produce any initial value distributions. The files written by `generate_initial` and needed by `fd3s` are `v0_r*`, `v0_phi*`, `v0_theta*`, `s0_phi_phi*`, `s0_phi_r*`, `s0_theta_phi*`, `s0_theta_r*`, `s0_theta_theta*` and `s0_r_r*`. The star * indicates that the file name is followed by the number of the process responsible for the particular region of the model that corresponds to the respective input file. Note that a complete set of initial value distributions is needed for each process.
Material parameters such as distributions of density and elastic parameters can be produced with the `fortan90` program `generate_models`. Standard output are the files `rhoinv*`, `lambda*`, `mu*`, `A*`, `B*` and `C*`, which contain the parameters necessary to describe a non-dissipative medium with radially symmetric anisotropy. Both programs `generate_initial` and `generate_models` take input from the file `model_parameters` which contains for example the model dimensions and the number of processes in each coordinate direction. Note that `model_parameters` should be consistent with the `Par` file.
The **source time function** can most conveniently be generated with the M-file `make_stf` which can be found in the `MATLAB` directory. It writes a file called `stf` into the `MODELS` directory, where `fd3s` expects it to be.
Receiver locations must be contained in the file `recfile`, located in the main directory. Since all receivers are assumed to be at the surface, `recfile` only includes the number of receivers and then always one row with the θ coordinate followed by the φ coordinate of the receiver. The maximum number of receivers should be set in the source file `fd3s_modules`.

3.4 Parallelisation

The parallelisation of `fd3s` is achieved by subdividing the model space

$$M = [\theta_{min}, \theta_{max}] \times [\varphi_{min}, \varphi_{max}] \times [r_{min}, r_{max}] \tag{71}$$

into smaller subspaces

$$M_{ijk} = [\theta_i, \theta_{i+1}] \times [\varphi_j, \varphi_{j+1}] \times [r_k, r_{k+1}]\,, \tag{72}$$

each of which is treated by one processor. The multi-index (ijk) and the single index

$$n = (k-1)n_\varphi n_\theta + (j-1)n_\theta + i \tag{73}$$

are assigned to the different subspaces following the scheme illustrated in figure (3).

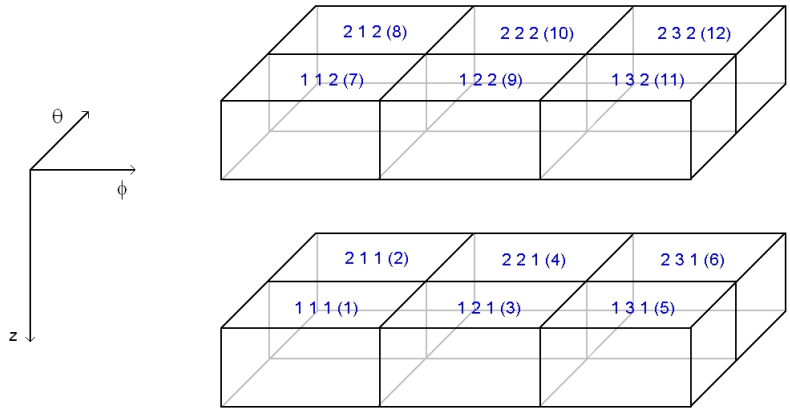

Figure 3: Organisation of the model subspaces M_{ijk}. The single index n corresponding to the multi-index (ijk) is given in parentheses.

The symbols n_φ and n_θ denote the number of subspaces in φ and θ direction, respectively. Both the multi-index and the single index are used in `fd3s`.
The subdivision of the model space M into subspaces M_{ijk} can conveniently be achieved by using the programme `generate_models` contained in the `MODELS` directory. All relevant parameters, such as the total model size and the number of processes in the different directions, are specified in the file `model_parameters`. Besides the files containing the physical model parameters and the initial values, `model_parameters` also generates a file named `boxfile`. It contains the dimensions of the different subspaces as well as their multi and single indeces. `boxfile` is also a necessary input for `fd3s`. It is important to make sure that the `Par` file and `boxfile` are consistent, meaning that they should give the same model size in all directions.

For the effectiveness of `fd3s` it is crucial that the maximum subspace size specified in the source file `fd3s_modules.f90` is not significantly larger than the maximum size of the subspaces in `boxfile`.

Solving the discretised version of the elastic wave equation requires the computation of discretised derivatives. For this, the stress and displacement fields at two neighboring points of each grid point have to be known. Consequently, the two-point boundary regions of the stress and displacement fields have to be sent from one subspace to its neighbours. If there are no neighbours, the stress and displacement fields have to be tapered at the boundaries, as prescribed by the implementation of the absorbing boundary condition. Those tasks are fulfilled by the two subroutines included in the source file `fd3s_comm_tap.f90`. For each coordinate direction, the subroutines check for the presence of a neighbour. If the test is positive, the boundaries of the stress and displacement fields are sent to the neighbour. In the next step, the boundaries of the stress and displacement fields sent by that neighbour are received and stored. If no neighbour is present, the fields are tapered.

3.5 Output files

The output in the form of wavefield snapshots and seismograms is written into the directory `DATA/OUTPUT`. Generally, each process produces its own output files. Hence, there are three files containing seismograms for each processor. (One file for each coordinate direction.) If there are no receivers located in a specific subspace, then the seismogram files are empty. The wavefield snapshots are generated for planes of constant r, φ and θ, respectively. Also this is done for each subspace.

4 Evaluation

4.1 Numerical body wave dispersion

Body waves in an entirely homogeneous and non-dissipative medium are not dispersive, i.e., their phase speeds do not depend on their frequency. The discretisation of the wave equation however introduces numerical dispersion of body waves that has no physical origin. Since an analytical evaluation of the numerical dissipation is difficult, especially in spherical coordinates, we will measure it directly using a technique similar to the one described in Dziewonski et al. (1969) and Dziewonski et al. (1972). A detailed description of the procedure can be found in Appendix A. It basically follows four steps:

1 Computation of the Fourier transform of the seismic signal $u(t)$, in our case a radial component velocity seismogram.

2 Multiplication of the transformed signal $u(\omega)$ by the Gaussian

$$g(\omega) = \exp\left[-\alpha \frac{(\omega - \omega_n)^2}{\omega_n^2}\right] . \tag{74}$$

3 Computation of the inverse Fourier transform in order to obtain the filtered signal $\bar{u}(\omega_n, t)$, which is generally complex.

4 The time t_n where $|\bar{u}(\omega_n, t)|$ attains its maximum, is equal to $k'(\omega_n)\, x$. The symbols $k'(\omega_n)$ and x denote the inverse group speed for the frequency ω_n and the distance between source and receiver, respectively.

It is important to note that this technique requires the wave number k to be linearisable about the frequency ω_n. Since we expect the numerical dispersion to be generally small, we assume that this requirement is satisfied. Therefore we can expect to obtain good estimates of the frequency dependent traveltimes of body waves.

We shall study the simple and easily reproducible case of a homogeneous and isotropic medium. The material parameters are $\mu = 8.00 \cdot 10^{10}$ N·m^{-2}, $\lambda = 1.19 \cdot 10^{11}$ N·m^{-2}, $\rho = 3543.25$ kg·m^{-3}, resulting in a P-wave speed of $c_p = 8873.63$ m·s^{-1} and an S-wave speed of $c_s = 4751.64$ m·s^{-1}. A single force in radial direction is located at a depth of 600.00 km, and also the receivers are at a depth of 600 km. This allows us to observe both direct and surface-reflected waves, and therefore to separate the numerical dispersion in the interior from the numerical dispersion caused by the free surface which is implemented only correct to second order in space. (The spatial derivatives in the interior of the medium are all correct to fourth order.) The parameters of the numerical model are summarised in the next table. The

$\Delta\theta$ [°]	$\Delta\varphi$ [°]	Δr [km]	Δt [s]
0.1	0.1	10.0	0.5

Table 1: Parameters of the numerical model. The spherical section is centred on the equator.

absolute effects of numerical dispersion depend very much on the number of grid points per wavelength. We therefore study two cases with distinct source time functions, both of the form

$$f(t) = \exp\left[-\frac{(t - t_p)^2}{t_s^2}\right] \tag{75}$$

but with different parameters t_s and t_p. See the following table for details. Both the derivative of the source time functions and their spectra are shown in figure (4).

Clearly, this choice of the source time function is to a certain extent arbitrary. Choosing a different function will result in different absolute discretisation errors. Therefore, the results obtained in this section are not very general. Nevertheless, they allow us to infer the order of magnitude of the numerical body wave dispersion.
Since the half-width $\Delta\omega = 2\pi\,\Delta\nu$ of the filter (74) greatly influences the dispersion measurements, we analysed the cases of $\Delta\nu_1 = 5$ mHz, $\Delta\nu_2 = 10$ mHz and $\Delta\nu_3 = 20$ mHz. Those

t_p $[s]$	t_s $[s]$	ν_{dominant} $[Hz]$	P-wave $\lambda_{\text{dominant}}$ $[km]$	S-wave $\lambda_{\text{dominant}}$ $[km]$
20.0	7.5	0.03	295	158
40.0	11.3	0.02	493	238

Table 2: Wavelet parameters t_p and t_s together with the respective dominant frequencies and wavelengths of the velocity field.

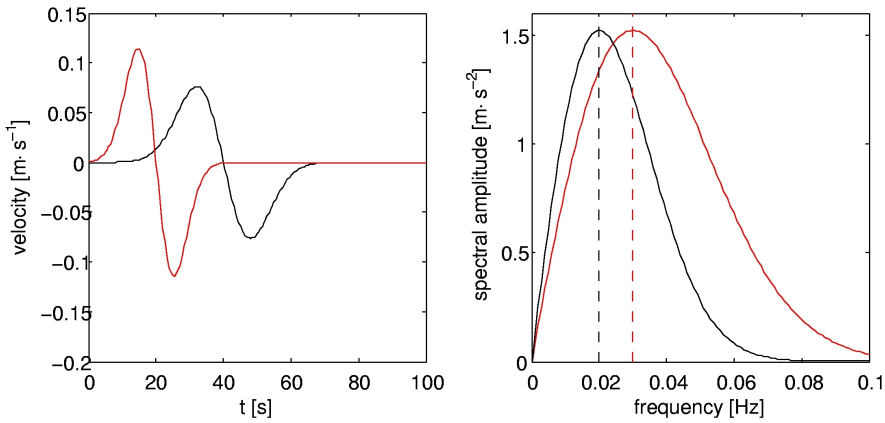

Figure 4: **Left**: Time derivative of the source time functions. The shapes of these functions will be reproduced in the velocity seismograms. (red: $t_p = 20.0$ s, $t_s = 7.5$ s; black: $t_p = 40.0$ s, $t_s = 11.3$ s) **Right**: Spectra of the functions on the left. The dominant frequencies of 0.02 Hz and 0.03 Hz, respectively, are indicated by vertical dashed lines.

seem to be reasonable values because the dominant frequencies are 20 mHz and 30 mHz, respectively. Choosing $\Delta\nu$ large, results in a poor frequency localisation and in a precise time localisation. The opposite is true for small values of $\Delta\nu$, where the determination of the amplitude maximum of the filtered signal becomes unstable.

In the case of a dominant frequency of 30 mHz ($t_s = 2.7$ s, $t_p = 20.0$ s), we observe that the arrival times of the direct P-wave differ by 2.0 per cent, given that the filter width is $\Delta\nu = 10$ mHz. (See figure (5).) This translates to wave speed variations of 2.3 per cent. The traveltime variations of the surface-reflected pP arrival amount to 4.0 per cent. Since the travelled distance of the pP phase is almost twice as long as that of the P phase, the wave speed variations are also on the order of 2 per cent. From this one may conclude that the relatively inaccurate treatment of the free surface does not have a major effect.

Since the spatial wavelength of S waves is shorter than the one of P waves, the S wave dispersion is generally larger, as indicated by figure (6). For the direct S phase the arrival times differ by approximately 5 in a frequency range from 10.0 mHz to 60.0 mHz. This translates to group speed variations of slightly less than 5 per cent. Similar values for the group speed variations are found for the surface reflected sS phase. This again suggests that the relatively inaccurate free-surface implementation does not significantly degrade the quality of the numerical solution.

In the case of a dominant frequency of 20 mHz, the relevant frequency band is narrower than for a dominant frequency of 30 mHz. This results in an apparently reduced numerical dispersion (see figure (7)). Quantitatively however, the arrival times in the reduced band from 15 mHz to 45 mHz differ by the same amount as in the case of a dominant frequency of 30 mHz. This implies that the effect of numerical dispersion can most effectively be reduced by propagating waves that are as monochromatic as possible, and to correct then for the wave speed discrepancy.

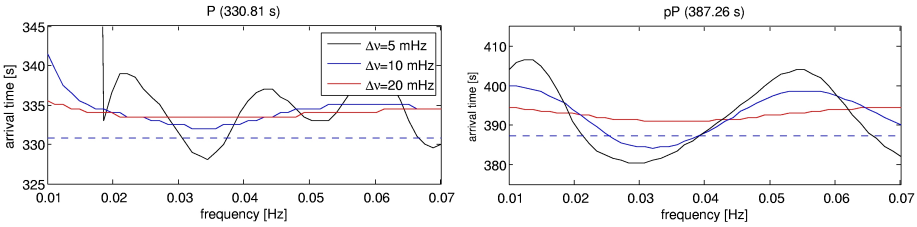

Figure 5: **Left**: Frequency-dependent arrival times of the direct P wave with a dominant frequency of 30 mHz for different filter widths $\Delta\nu$. The ray-theoretical arrival time of 330.81 s is indicated by a dashed line. **Right**: Frequency-dependent arrival times of the surface-reflected pP phase. The ray-theoretical arrival time is 387.26 s.

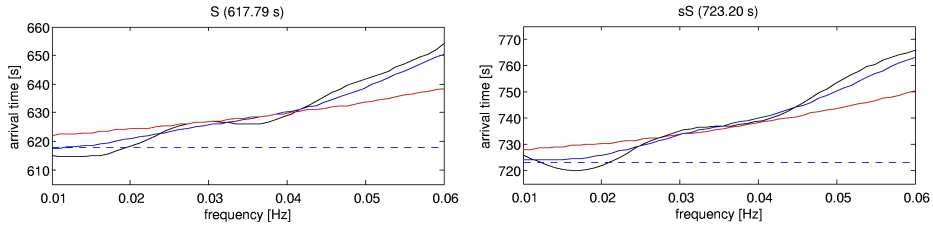

Figure 6: **Left**: Frequency-dependent arrival times of the direct S wave with a dominant frequency of 30 mHz for different filter widths $\Delta\nu$. The ray-theoretical arrival time of 617.79 s is indicated by a dashed line. **Right**: Frequency-dependent arrival times of the surface-reflected sS phase. The ray-theoretical arrival time is 723.20 s.

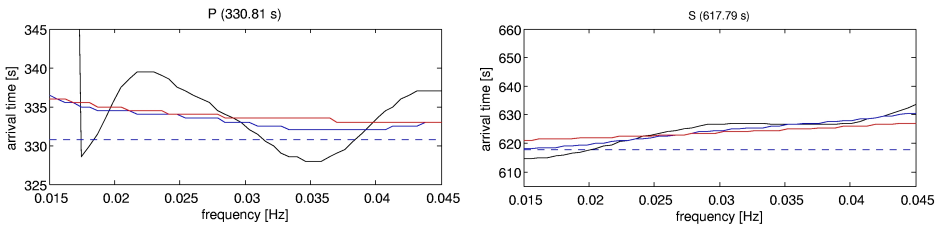

Figure 7: **Left**: Frequency-dependent arrival times of the direct P wave with a dominant frequency of 20 mHz for different filter widths $\Delta\nu$. The ray-theoretical arrival time of 330.81 s is indicated by a dashed line. **Right**: Frequency-dependent arrival times of the direct S wave with a dominant frequency of 20 mHz for different filter widths $\Delta\nu$. The ray-theoretical arrival time of 617.79 s is indicated by a dashed line.

4.2 Elastic waves in the Preliminary Reference Earth Model (PREM)

The accuracy of synthetically computed body wave traveltimes for realistic Earth models is of particular importance. For several reasons body wave traveltimes are the most important seismic information used for both source and structural inversion. Traveltimes depend linearly on large-scale Earth structures and are robust with respect to erroneous receiver calibration and orientation.

To evaluate the accuracy of traveltimes computed with `fd3s` we adopt the material parameters provided by the Preliminary Reference Earth Model (PREM), proposed by Dziewonski & Anderson (1981). We neglect both anisotropy and attenuation. In PREM anisotropy with radial symmetry axis is confined to the upper 220 km. It therefore primarily affects surface waves. Body waves recorded at epicentral distances travel almost vertically through the upper 220 km and therefore remain largely unaffected by anisotropy with radial symmetry axis.

A first qualitative check of the wavefield is provided in figure (8). It shows a wavefield snapshot in PREM, $3:30$ min after the initiation of the source, which acted at a depth of 400 km. The model extension is $60°$ in ϕ direction, $30°$ in θ direction and 2000 km in depth. The direct S wave and its surface reflection are clearly visible on the cut in ϕ direction. The direct P wave can be observed only on the surface due to its small amplitude in deeper parts of the model where the P wave speed increases rapidly. The most prominent feature of the wavefield snapshot are the surface waves which decay quickly with depth.

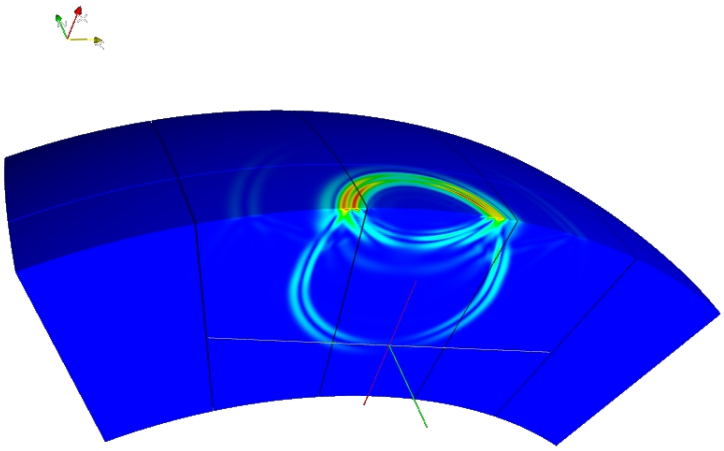

Figure 8: Snapshot of the velocity field amplitude $||\mathbf{v}||$ in PREM, $3:30$ min after the source initiation at a depth of 400 km. The image is dominated by the surface waves which decay rapidly with depth. Also the direct S wave and its surface reflection are clearly visible. Due to its small amplitude, the direct P wave can be observed only on the surface.

A more quantitative evaluation is illustrated in figure (9), which shows a radial component synthetic seismogram at an epicentral distance of 60°. The dominant period is 30 s. Some prominent arrivals appear during the first 20 minutes, among them P, PP, PPP, PcP, PcS. Around 60° the direct S wave interferes with the PS phase, and also PPS should become visible. Shortly after S one can expect ScS. However, due to the relatively long period, it is only the S arrival which is clearly visible. The smaller PS, PPS and ScS arrivals can not be distinguished.
The arrival times of P, PP, PPP, PcP, PcS and S are all within 1 s of the ray theoretical arrival times for PREM. Given the difficulties in measuring the exact onset of a long-period wave and the relatively long time increment of $\Delta t = 0.35$ s, this error is small.

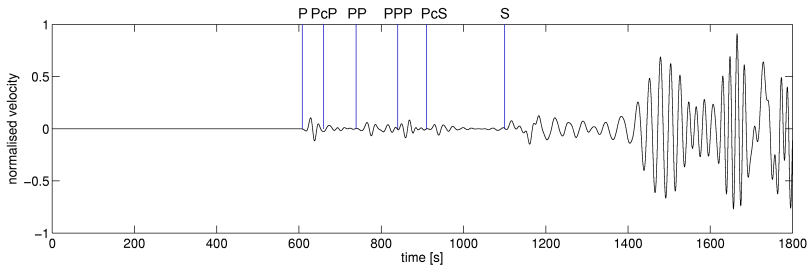

Figure 9: Synthetic radial component seismogram at an epicentral distance of 60°. The arrivals of some prominent phases such as P. PP, PPP. PcP. PcS and S are clearly visible. Their traveltimes agree well with the ray-theoretical predictions.

At this point it is important to note that the correct localisation of discontinuities such as the core-mantle boundary is of particular importance. A radial grid spacing that is too wide can easily misplace discontinuities significantly and therefore lead to inaccurate arrival times of reflected waves.

A Appendix A - Dispersion measurements

In the following lines we will briefly outline the technique used to measure numerical dispersion. A similar procedure was developed by Dziewonski et al. (1969) and Dziewonski et al. (1972) for the purpose of surface wave dispersion measurements.

The recording $f(t)$ of a wave travelling through a dispersive medium may be represented as

$$f(t) = \int_{-\infty}^{\infty} F(\omega) e^{-\mathbf{i}k(\omega)x} e^{\mathbf{i}\omega t}\, dt = \int_{-\infty}^{\infty} |F(\omega)| e^{\mathbf{i}\phi(\omega)} e^{-\mathbf{i}k(\omega)x} e^{\mathbf{i}\omega t}\, dt = \int_{-\infty}^{\infty} f(\omega) e^{\mathbf{i}\omega t}\, dt\,. \quad (76)$$

The spectrum $F(\omega)$ is usually unknown, but the spectrum $f(\omega)$ may be obtained through a Fourier transform of the signal $f(t)$. Instead of the signal itself, we shall consider the signal filtered with a Gaussian centered at the frequency ω_n, i.e.,

$$f_n(t) := \int_{-\infty}^{\infty} f(\omega) e^{-\alpha(\omega-\omega)^2/\omega_n^2} e^{\mathbf{i}\omega t}\, dt\,. \quad (77)$$

Under the assumption that $|F(\omega)|$, $\phi(\omega)$ and $k(\omega)$ can be reasonably linearized about the frequency ω_n, we find after a laborious but straightforward calculation that f_n is given by

$$f_n(t) = \omega_n \sqrt{\frac{\pi}{\alpha}} \left[|F(\omega_n)| - \frac{\omega_n}{\sqrt{\alpha}} b |F(\omega_n)|' \right] \exp\left[-\mathbf{i}\bar{k}(\omega_n)x + \mathbf{i}\omega_n t\right] \exp\left[-\frac{\omega_n^2}{4\alpha}\left(\bar{k}'(\omega_n)x - t\right)^2\right], \quad (78)$$

with

$$b := \frac{\mathbf{i}\omega_n}{2\sqrt{\alpha}} \left[\bar{k}'(\omega_n)x - t\right] \quad (79)$$

and

$$\bar{k}(\omega) := k(\omega) - \phi(\omega)/x\,. \quad (80)$$

The complex filtered signal $f_n(t)$ attains it maximum at

$$t = t_{max} := k'(\omega_n)x - \phi'(\omega_n)\,. \quad (81)$$

If x is sufficiently large, one may directly obtain the inverse group velocity $k'(\omega_n)$. Otherwise, one has to correct for $\phi'(\omega_n)$.

References

[1] Babuska, V., Cara, M., 1991. Seismic anisotropy in the Earth, *Kluwer Acad. Pub.*

[2] Blanch, J. O., Robertsson, J. O. A., Symes, W. W., 1995. Modeling of a constant Q: Methodology and algorithm for an efficient and optimally inexpensive viscoelastic technique, *Geophysics*, **60**(1), 176-184.

[3] Born, W. T., 1941. The attenuation constant of Earth materials, *Geophysics*, **6**, 132-148.

[4] Cerjan, C., Kosloff, D., Kosloff, R., Reshef, M., 1985. A nonreflecting boundary condition for discrete acoustic and elastic wave equations, *Geophysics*, **50**(4), 705-708.

[5] Cheng, H.-X., Kennett, B. L. N., 2002. Frequency dependence of seismic wave attenuation in the upper mantle beneath the Australian region, *Geophys. J. Int.*, **150**, 45-57.

[6] Dahlen, F. A., J. Tromp, 1998. Theoretical Global Seismology, *Princeton Univ. Press.*

[7] Dziewonski, A. M., Bloch, S., Landisman, L., 1969. A technique for the analysis of transient seismic signals, *Bull. Seism. Soc. Am.*, 59(1), 427-444.

[8] Dziewonski, A. M., Mills, J., Bloch, S., 1972. Residual dispersion measurement - a new method of surface-wave analysis, *Bull. Seism. Soc. Am.*, 62(1), 129-139.

[9] Dziewonski, A. M., Anderson, D. L., 1981. Preliminary Reference Earth Model, *Phys. Earth Planet. Int.*, **25**, 297-356.

[10] Eckström, G., Dziewonski, A. M., 1998. The unique anisotropy of the Pacific upper mantle, *Nature*, **394**, 168-172.

[11] Gung, Y., Romanowicz, B., 2004. Q tomography of the upper mantle using three-component long-period waveforms, *Geophys. J. Int.*, **157**, 813-830.

[12] Igel, H., Mora, P., Riollet, B., 1995. Anisotropic wave propagation through finite-difference grids, *Geophysics*, **60**(4), 1203-1216.

[13] Igel, H., Nissen-Meyer, T., Jahnke, G., 2002. Wave propagation in 3-D spherical sections: Effects of subduction zones, *Phys. Earth Planet. Inter.*, **132**, 219-234.

[14] Jackson, I., 2000. Laboratory measurements of seismic wave dispersion and attenuation: Recent progress, in *Earth's Deep Interior: Mineral Physics and Tomography from the Atomic to the Global Scale*, Geophysical Monograph 117, S. Karato (eds), 265-289.

[15] Kirkpatrick, S., Gelatt, C. D., Vecchi, M. P., 1983. Optimization by Simulated Annealing, *Science*, **220**, 671-680.

[16] Love, A. E. H., 1892. The mathematical theory of elasticity, *Cambridge Univ. Press.*

[17] Nissen-Meyer, T. F., 2001. Numerical simulation of 3-D seismic wave propagation through subduction zones, *Diploma thesis*, Ludwig-Maximilians-Universität München.

[18] Robertsson, J. O. A., Blanch, J. O., Symes, W. W., 1994. Viscoelastic finite-difference modeling, *Geophysics*, **59**(9), 1444-1456.

[19] Romanowicz, B., Durek, J. J., 2002. Seismological constraints on attenuation in the Earth: A review, in *Earth's Deep Interior: Mineral Physics and Tomography from the Atomic to the Global Scale*, Geophysical Monograph 117, S. Karato (eds), 161-180.

[20] Schade, H., 1999. Tensoranalysis, *DeGruyter.*

[21] Shito, A., Karato, S., Park, J., 2004. Frequency dependence of Q in the Earth's upper mantle inferred from continuous spectra of body waves, *Geophys. Res. Lett.*, **31**, L12603, doi:10.1029/2004GL019582.

[22] Virieux, J., 1984. SH-wave propagation in heterogeneous media: Velocity-stress finite-difference method, *Geophysics*, **49**, 1933-1957.